

This is the author's peer reviewed, accepted manuscript. However, the online version of record will be different from this version once it has been copyedited and typeset.

PLEASE CITE THIS ARTICLE AS DOI: 10.1063/5.0165555

*Accepted to Phys. Fluids 10.1063/5.0165555*

1 **A numerical study of the settling of non-spherical particles in quiescent water**

2 Xiaoyong Cheng (程潇勇)<sup>1</sup>, Zhixian Cao (曹志先)<sup>1,a)</sup>, Ji Li (李季)<sup>2</sup>, Alistair Borthwick<sup>3,4</sup>

3

4 AFFILIATIONS

5 <sup>1</sup>State Key Laboratory of Water Resources Engineering and Management, Wuhan  
6 University, Wuhan 430072, China

7 <sup>2</sup>Zienkiewicz Centre for Computational Engineering, Faculty of Science and Engineering,  
8 Swansea University, Swansea SA1 8EN, UK

9 <sup>3</sup>Institute for Infrastructure and Environment, The University of Edinburgh, Edinburgh  
10 EH9 3JL, UK

11 <sup>4</sup>School of Engineering, Computing and Mathematics, University of Plymouth, Plymouth  
12 PL4 8AA, UK

13

14 <sup>a)</sup>Author to whom correspondence should be addressed: zxcao@whu.edu.cn

15

## 16 ABSTRACT

17 The settling of non-spherical particles is poorly understood, with previous studies  
 18 having focused mainly on spherical particles. Here, a series of particle-resolved direct  
 19 numerical simulations are conducted using FLOW-3D (commercial computational fluid  
 20 dynamics software) for spheres and five regular, non-spherical shapes of sediment  
 21 particles, i.e., prolate spheroid, oblate spheroid, cylinder, disk, and cube. The Galileo  
 22 number varies from 0.248 to 360 and the particle Reynolds number  $Re_p$  ranges from  
 23 0.00277 to 562. The results show that a non-spherical particle may experience larger drag  
 24 and consequently attain a lower terminal velocity than an equivalent sphere. If  $Re_p$  is  
 25 sufficiently small, the terminal velocity is less affected by particle shape as characterized  
 26 by the particle aspect ratio. For relatively large  $Re_p$ , the shape effect (represented by the  
 27 Corey shape factor) becomes more significant. Empirical correlations are derived for the  
 28 dimensionless characteristic time  $t_{95^*}$  and displacement  $s_{95^*}$  of particle settling, which  
 29 show that  $t_{95^*}$  remains constant in the Stokes regime ( $Re_p < 1$ ) and decreases with  
 30 increasing  $Re_p$  in the intermediate regime ( $1 \leq Re_p < 10^3$ ), whereas  $s_{95^*}$  increases  
 31 progressively with increasing  $Re_p$  over the simulated range. It is also found that in the  
 32 Stokes regime, particle orientation remains essentially unchanged during settling, and so  
 33 the terminal velocity is governed by the initial orientation. In the intermediate regime, a  
 34 particle provisionally settling at an unstable orientation self-readjusts to a stable  
 35 equilibrium state, such that the effect of initial orientation on the terminal velocity is  
 36 negligible. Moreover, an unstable initial orientation can enhance the vertical displacement  
 37 and may promote vortex shedding.

38

## 39 I. INTRODUCTION

40 The settling of particles in fluids is key to many natural and industrial processes,  
 41 such as sediment dynamics in alluvial rivers,<sup>1,2</sup> transportation of marine microplastics,<sup>3,4</sup>  
 42 proppant settling in hydraulic fractures,<sup>5,6</sup> and chemical and powder processing.<sup>7</sup>  
 43 Although particulate flows are generally turbulent and involve large amounts of particles,  
 44 an improved understanding of the settling of a single particle in quiescent fluid is a  
 45 prerequisite for modelling complex particle-laden turbulent flows. However, most  
 46 existing models of particulate flows assume the grains to be spheres when in fact the most  
 47 commonly encountered particles in practical applications are non-spherical.<sup>8,9</sup> Such  
 48 simplification inevitably ignores the key roles played by particle shape and orientation in  
 49 the settling process. Studies are urgently needed to gain better insight into the settling of  
 50 non-spherical particles in quiescent water.

51 When a heavy particle falls through a static fluid, the particle accelerates due to  
 52 gravity and increasing fluid drag is exerted on its surface. As the submerged weight of the  
 53 particle is balanced by fluid drag, its acceleration terminates, enabling the particle to fall  
 54 at a nearly constant velocity, called the terminal velocity. The drag force is one of the  
 55 fundamental forces that affect the settling process, which can be defined as

$$56 \quad F_d = \frac{1}{2} C_d \rho_f W^2 \frac{\pi}{4} d_n^2, \quad (1)$$

57 where  $C_d$  is the drag coefficient;  $\rho_f$  is the fluid density;  $W$  is the settling velocity;  
 58 and  $d_n$  is the diameter of a sphere of equivalent volume to that of the particle. Accurate  
 59 estimates of settling velocity and drag coefficient are of particular importance because  
 60 other parameters can be readily inferred. Notably, the terminal velocity of a particle,  
 61 denoted  $W_t$ , can be simply derived by equating the drag force to the submerged weight

This is the author's peer reviewed, accepted manuscript. However, the online version of record will be different from this version once it has been copyedited and typeset.

PLEASE CITE THIS ARTICLE AS DOI: 10.1063/5.0165555

Accepted to *Phys. Fluids* 10.1063/5.0165555

62 of the particle. The drag coefficient  $C_d$  in Eq. (1) is however very challenging to  
 63 determine because it depends on many parameters including the particle Reynolds  
 64 number and particle shape.<sup>10</sup> Herein, the particle Reynolds number is defined as  
 65  $Re_p = Wd_n / \nu$ , with  $\nu$  being the kinematic viscosity. Except at sufficiently small  $Re_p$ ,  
 66 where an analytical solution exists for spheres based on Stokes' law, in which  $C_d$  is  
 67 inversely proportional to  $Re_p$ , no general solution can be found for determining the drag  
 68 coefficient of particles of any shape. Based on a large number of theoretical and  
 69 experimental investigations of settling behavior, numerous empirical models have been  
 70 developed to predict the drag coefficient and settling velocity of spherical particles<sup>11-13</sup>  
 71 and non-spherical particles.<sup>14-18</sup> To account for the shape effect of non-spherical particles,  
 72 various approaches have been proposed to define particle shape. Of these, the Corey shape  
 73 factor<sup>19</sup> (CSF) is the most commonly used shape descriptor,<sup>14,20,21</sup> and is defined as  
 74  $CSF = d_s / \sqrt{d_m d_l}$ , where  $d_s$ ,  $d_m$ , and  $d_l$  are respectively the shortest, intermediate,  
 75 and longest form dimensions of the particle. Sphericity  $\phi$  is another widely used shape  
 76 descriptor,<sup>15,22,23</sup> and is given by the ratio of the surface area of the volume-equivalent  
 77 sphere to that of the actual particle. Circularity  $X$  is the ratio of the perimeter of the  
 78 maximum projection area of the particle to the perimeter of a circle that has area equal to  
 79 the maximum projection area. This descriptor is able to reflect the irregularity of particle  
 80 contours and is thus very suitable for particles with sharp corners and large obtuse  
 81 angles.<sup>24</sup> In addition, for highly irregular particles, the parameter  $\xi$ , which is the ratio  
 82  $\phi / X$ , is another effective shape descriptor.<sup>17,25,26</sup> However, these aforementioned  
 83 empirical models cannot provide sufficient effective information to quantify the whole  
 84 process of particle settling. Consequently, the time and space scales that are required for  
 85 a particle to reach its terminal settling state have not yet been resolved.

86 Particle orientation also has a vital effect on settling non-spherical particles. In  
 87 general, a non-spherical particle could fall at any orientation without rotation at  
 88 sufficiently small  $Re_p$ ,<sup>27,28</sup> but will assume a stable orientation and tend to fall with the  
 89 maximum projection area normal to the direction of settling motion at relatively large  
 90  $Re_p$ .<sup>8,29</sup> Besides, particle orientation can appreciably modify the drag coefficient.<sup>16,18</sup>  
 91 Over the past decade, particle-resolved direct numerical simulation (PR-DNS) has been  
 92 carried out to establish correlations between  $C_d$  and particle orientation.<sup>30-33</sup> However,  
 93 such correlations are based on the assumption of a stationary obstacle exposed to a  
 94 moving fluid, therefore neglecting the effects of secondary motions and wake structures.<sup>34</sup>  
 95 Moreover, most existing numerical studies considering the influence of particle  
 96 orientation on free settling have been confined to two-dimensional modeling.<sup>35-37</sup> Overall,  
 97 there is a need for a three-dimensional model that can properly address the effect of  
 98 particle orientation on the settling process of non-spherical particles.

99 The present work sets out to unravel the effects of particle shape and initial  
 100 orientation on the settling of non-spherical sediment particles in quiescent water. Using  
 101 the commercial computational fluid dynamics (CFD) software FLOW-3D (version 11.2),  
 102 a series of PR-DNS simulations are performed for a range of particle sizes, shapes, and  
 103 distinct initial orientations. Based on the computational results, key parameters that  
 104 characterize the settling process, including terminal velocity  $W_t$  and drag coefficient  
 105  $C_d$ , are analyzed to reveal the influence of particle shape on settling. Furthermore, the  
 106 time and space scales required to reach terminal settling are also investigated. In addition,  
 107 the settling processes of non-spherical particles in the Stokes and intermediate regimes  
 108 are presented, thereby probing into the effect of initial particle orientation.

109 II. METHOD

110 A. Computational fluid dynamics (CFD) model

111 The commercial CFD software FLOW-3D, developed by Flow Science, is used to  
 112 conduct PR-DNS simulations of particle settling in otherwise quiescent fluid. FLOW-3D  
 113 utilizes a fractional area/volume obstacle representation (FAVOR) technique<sup>38</sup> and  
 114 provides a general moving object model that can simulate rigid body motion that is  
 115 dynamically coupled with fluid flow. The FAVOR method defines complicated geometric  
 116 shapes through fractional areas and volumes within rectangular elements and has been  
 117 proven to be one of the most efficient methods to treat immersed solid bodies.<sup>39,40</sup>

118 Assuming the fluid to be incompressible, the continuity and momentum equations  
 119 based on the FAVOR method are given as

120 
$$\frac{\partial U_i}{\partial x_i} = -\frac{\partial V_f}{\partial t}, \quad (2)$$

121 
$$\frac{\partial u_i}{\partial t} + \frac{U_j}{V_f} \frac{\partial u_i}{\partial x_j} = -\frac{1}{\rho_f} \frac{\partial p}{\partial x_i} + g_i + f_i, \quad (3)$$

122 where subscripts  $i$  and  $j=1,2,3$  denote  $x$ ,  $y$ , and  $z$  directions;  $x_i$  are Cartesian  
 123 coordinates;  $t$  is time;  $U_i = u_i A_i = (uA_x, vA_y, wA_z)$  in which  $u_i$  is the  $i$ -th velocity  
 124 component and  $A_i$  is the corresponding area fraction;  $V_f$  is volume fraction;  $p$  is  
 125 pressure;  $g_i$  is the  $i$ -th body acceleration component; and  $f_i$  is the  $i$ -th viscous  
 126 acceleration component. The viscous acceleration components in Eq. (3) are calculated  
 127 as

128 
$$f_i = \frac{1}{\rho_f V_f} \left( w s x_i - \frac{\partial T_{ij}}{\partial x_j} \right), \quad (4)$$

129 where  $w_{sx_i}$  are wall shear stress components; and  $T_{ij} = A_{\perp} \tau_{ij} = -2A_{\perp} \mu (s_{ij} - s_{kk} \delta_{ij} / 3)$ , in  
 130 which  $\mu$  is dynamic viscosity,  $s_{ij} = (\partial u_i / \partial x_j + \partial u_j / \partial x_i) / 2$  is the strain rate tensor,  
 131 and  $\delta_{ij}$  is the Kronecker delta function. Compared to the continuity equation applied in  
 132 stationary obstacle problems,  $-\partial V_f / \partial t$  on the right-hand side of Eq. (2) is equivalent to  
 133 an additional volume source term and exists solely in mesh cells around the boundary of  
 134 the moving object. The term is evaluated as

$$135 \quad -\frac{\partial V_f}{\partial t} = \frac{S_{\text{obj}}}{V_{\text{cell}}} V_{\text{obj}} n_i, \quad (5)$$

136 where  $V_{\text{cell}}$  is the volume of a mesh cell;  $S_{\text{obj}}$ ,  $n_i$ , and  $V_{\text{obj}}$  are respectively the  
 137 surface area, unit normal vector, and velocity of the moving object in the mesh cell.

138 According to kinematics, the general motion of a rigid body can be divided into  
 139 translational motion and rotational motion components. Newton's second law describes  
 140 the translational motion of a rigid body as

$$141 \quad m_p \frac{d\mathbf{V}_G}{dt} = \mathbf{F}, \quad (6)$$

142 where  $\mathbf{V}_G$  is the mass center velocity of the rigid body;  $\mathbf{F}$  is the total force on the body;  
 143 and  $m_p$  is rigid body mass. Euler's equation describes rigid body rotation in a frame of  
 144 reference fixed at the centroid of the rotating body as

$$145 \quad \mathbf{I} \frac{d\boldsymbol{\omega}}{dt} + \boldsymbol{\omega} \times (\mathbf{I}\boldsymbol{\omega}) = \mathbf{T}_G, \quad (7)$$

146 where  $\boldsymbol{\omega}$  is the angular velocity of the rigid body;  $\mathbf{I}$  is the diagonal inertia matrix  
 147 relative to the principal axes of the rigid body; and  $\mathbf{T}_G$  is the total torque about the mass  
 148 center. The present paper considers the free settling of a single particle, so the total force  
 149 and total torque include only hydrodynamic and gravitational forces and torques.

150 The CFD model solves the governing equations of fluid motion [Eqs. (2) and (3)]  
 151 using a finite volume/finite difference method.<sup>41</sup> Pressures and velocities are coupled  
 152 implicitly and solved by using a generalized minimal residual method, which is the  
 153 default solver of FLOW-3D. The momentum advection algorithm adopts a first-order  
 154 upwind scheme. For coupled rigid body motion [Eqs. (6) and (7)], both the explicit and  
 155 implicit general moving objects methods work well since heavy object problems are  
 156 considered in the present paper.

157

#### 158 B. Study cases

159 A series of numerical cases are used to investigate the influences of particle shape  
 160 and initial orientation on the settling of non-spherical particles. Table I summarizes the  
 161 simulation parameters. In all cases, the fluid is specified as water at 20 °C ( $\rho_f = 1000$   
 162 kg/m<sup>3</sup>,  $\nu = 1 \times 10^{-6}$  m<sup>2</sup>/s), and the particles are assumed to be composed of siliciclastic  
 163 sediment of homogeneous density 2650 kg/m<sup>3</sup>. Eight spherical equivalent diameters are  
 164 considered, i.e.,  $d_n = 0.015625, 0.03125, 0.0625, 0.125, 0.25, 0.5, 1,$  and 2 mm.  
 165 Consequently, the value of the Galileo number varies from 0.248 to 360. The Galileo  
 166 number  $Ga$  is the ratio between gravitational and viscous forces, and is defined as

$$167 \quad Ga = \frac{\sqrt{(\rho_p / \rho_f - 1) g d_n^3}}{\nu}, \quad (8)$$

168 where  $\rho_p$  is particle density; and  $g$  is gravitational acceleration. As indicated in Table  
 169 II, six particle shapes are considered, including spheres and five regular non-spherical  
 170 shapes, i.e., prolate spheroid, oblate spheroid, cylinder, disk, and cube, with the first four  
 171 shapes being axisymmetric. Although particles in natural and industrial processes are  
 172 generally irregular, it is justified to choose regular non-spherical particles as the object of



173 the present study because the most accurate previous models for predicting the behavior  
 174 of non-spherical particles in fluids were based on studies of regular particles, for which  
 175 characterization of particle shape is not complex.<sup>18</sup>

176 Among the parameters listed in Table I,  $\beta$  is defined as the angle between the plane  
 177 in which the maximum projection area of a particle lies and the horizontal plane  
 178 perpendicular to the direction of settling motion (and thus provides a reasonable  
 179 description of the particle orientation).  $\beta_0$  denotes the initial orientation of a particle  
 180 upon release. As previously noted, a particle settling at sufficiently small  $Re_p$  exhibits  
 181 no preferred orientation. If  $Re_p$  is relatively large, a particle tends to fall with its  
 182 maximum projection area normal to the direction of settling motion, i.e., at a state of  
 183  $\beta = 0^\circ$ . Therefore, the typical initial state of  $\beta_0 = 0^\circ$  is chosen to exclude any influence  
 184 of orientation variation; the combination of different particle sizes and shapes leads to 36  
 185 cases. A further 32 cases that consider two distinct initial orientations ( $\beta_0 = 45^\circ$  and  $90^\circ$ )  
 186 are simulated for axisymmetric particles with four selected spherical equivalent diameters  
 187 ( $d_n = 0.015625, 0.0625, 0.25, \text{ and } 1 \text{ mm}$ ). Overall, a total of 68 numerical cases are  
 188 considered, and the particle Reynolds number  $Re_p$  ranges from 0.00277 to 562,  
 189 covering both the Stokes regime ( $Re_p < 1$ ) and the intermediate regime ( $1 \leq Re_p < 10^3$ ).

190 In this paper, the Corey shape factor CSF is used to describe particle shape, noting  
 191 that CSF suffices for regular particles.<sup>42</sup> The projection area protocol, which is associated  
 192 with the lowest operator-dependent errors compared to other methods,<sup>43</sup> is applied to  
 193 determine the form dimensions of a given particle (see Table II). Particle settling is  
 194 simulated in a domain of dimensions  $8d_n \times 8d_n$  in the  $x$  and  $y$  directions. The size of the  
 195 domain in the  $z$ -direction is carefully determined to ensure the whole-process modeling

This is the author's peer reviewed, accepted manuscript. However, the online version of record will be different from this version once it has been copyedited and typeset.

PLEASE CITE THIS ARTICLE AS DOI: 10.1063/5.0165555

*Accepted to Phys. Fluids 10.1063/5.0165555*

196 of particle settling can be achieved without exceptional computational cost. A resolution  
197 of 12 grids per  $d_n$  is used, which can successfully resolve the geometry of both spherical  
198 and non-spherical particles considered in the present study. Periodic boundary conditions  
199 are imposed in the horizontal directions to mimic an unbounded domain without wall  
200 effect, and a free surface and a stationary wall are implemented at the upper and bottom  
201 boundaries. More information on the validation of the CFD model is given in the  
202 Appendix. In addition, a dual-Euler whole-attitude solver is used to reproduce the  
203 variation in orientation of particles, based on the time series of particle angular velocities  
204 output from the CFD model. A brief description of the method is given in the  
205 Supplementary Material.  
206

This is the author's peer reviewed, accepted manuscript. However, the online version of record will be different from this version once it has been copyedited and typeset.

PLEASE CITE THIS ARTICLE AS DOI: 10.1063/5.0165555

Accepted to Phys. Fluids 10.1063/5.0165555

207

208 **TABLE I.** Summary of simulation parameters.

$\rho_f$ (kg/m <sup>3</sup> )	$\nu$ (m <sup>2</sup> /s)	$\rho_p$ (kg/m <sup>3</sup> )	$d_n$ (mm)	$\beta_0$ (°)
1000	$1 \times 10^{-6}$	2650	0.015625-2	0, 45 and 90

209

210 **TABLE II.** Summary of six particle shapes considered in this work. Semi-axes lengths  
 211 of the ellipsoid are  $a$ ,  $b$ , and  $c$ ; the diameter and height of the cylinder and disk are  
 212  $d$  and  $h$  ( $d < h$  for the cylinder,  $d > h$  for the disk), respectively; and the edge  
 213 length of the cube is  $a$ .

Shape	$d_l$	$d_m$	$d_s$	CSF
Sphere	$d_n$	$d_n$	$d_n$	1.00
Ellipsoid 1 (prolate spheroid, $a = 4b = 4c$ )	$2a$	$2b$	$2c$	0.50
Ellipsoid 2 (oblate spheroid, $a = b = 2c$ )	$2a$	$2b$	$2c$	0.50
Cylinder ( $h = 2d$ )	$\sqrt{h^2 + d^2}$	$d$	$d$	0.67
Disk ( $h = 1/4d$ )	$\sqrt{h^2 + d^2}$	$d$	$h$	0.25
Cube	$\sqrt{3}a$	$\sqrt{2}a$	$a$	0.64

214

215

216 III. RESULTS AND DISCUSSION

217 A. Particle settling with maximum projection area normal to fall direction

218 1. Terminal settling state

219 The terminal settling state and terminal velocity of a particle are simultaneously  
 220 attained when the submerged weight of the particle is balanced by fluid drag. Terminal  
 221 velocity is a fundamental hydrodynamic parameter that both directly and indirectly  
 222 governs sedimentary processes.<sup>29</sup> Here, the terminal velocity  $W_t$  and spherical  
 223 equivalent diameter  $d_n$  are normalized following Dietrich<sup>14</sup>, such that:

224 
$$W_{t*} = \frac{\rho_f W_t^3}{(\rho_s - \rho_f) g V}, \quad (9)$$

225 
$$d_* = \frac{(\rho_s - \rho_f) g d_n^3}{\rho_f \nu^2}, \quad (10)$$

226 where  $W_{t*}$  is the dimensionless terminal velocity; and  $d_*$  is the dimensionless  
 227 spherical equivalent diameter. Figure 1 illustrates the variation in  $W_{t*}$  with  $d_*$  obtained  
 228 for different shapes when  $\beta_0 = 0^\circ$ . It appears that a non-spherical particle attains a lower  
 229 terminal velocity than its spherical counterpart, with the difference in terminal velocity  
 230 becoming increasingly evident as the particle size increases. This trend is further  
 231 confirmed in Fig. 2 which shows the variation in  $\delta$  with particle Reynolds number  $Re_p$   
 232 where  $\delta$  is defined as the relative deviation of the terminal velocity of a non-spherical  
 233 particle from that of its spherical counterpart with the same  $d_n$  as follows:

234 
$$\delta = \frac{W_t - W_{t\text{-sphere}}}{W_{t\text{-sphere}}} \times 100\%. \quad (11)$$

235 For a specific non-spherical particle shape,  $\delta$  remains essentially unchanged in the

236 Stokes regime, whereas  $\delta$  decreases progressively with increasing  $Re_p$  in the  
 237 intermediate regime. Figure 2 also shows that  $\delta$  varies with particle shape. In addition  
 238 to the CSF, the aspect ratio obtained by dividing  $d_l$  by  $d_s$  is selected here to account  
 239 for the shape effect. In the Stokes regime with low  $Re_p$ ,  $\delta$  is largely dependent on the  
 240 aspect ratio, with larger particle aspect ratio corresponding to smaller terminal velocity.  
 241 The foregoing observations indicate that the longest and shortest form dimensions may  
 242 govern terminal velocity in the Stokes regime. Therefore, elongated, flat particles may  
 243 reach almost equal values of terminal velocity despite their distinct shapes. When  $Re_p$   
 244 exceeds 10, the computed  $\delta$  generally decreases with decreasing CSF, and little  
 245 consistency is observed between  $\delta$  and the aspect ratio. In short, when the viscous force  
 246 dominates, the terminal velocity is less affected by the non-spherical particle shape, which  
 247 can be characterized by the particle aspect ratio. When the inertial force becomes  
 248 dominant, the shape effect tends to become significant, and should be represented by  
 249 CSF instead of aspect ratio.

250 Figure 3 illustrates the drag coefficient  $C_d$  as a function of particle Reynolds  
 251 number  $Re_p$ . Results obtained from the spherical drag law proposed by Clift and  
 252 Gauvin<sup>11</sup> are also included for comparison. The computed  $C_d$  curve for spheres exhibits  
 253 satisfactory agreement with Clift and Gauvin's empirical relationship, confirming the  
 254 validity of the present model. Non-spherical particles are predicted to experience  
 255 relatively larger drag than equivalent spheres, with the difference between drag  
 256 coefficient values progressively increasing as  $Re_p$  increases.

257 When a particle moves through a fluid, the total drag exerted on its surface can be  
 258 divided into pressure drag (or form drag)  $F_{pd}$  and friction drag  $F_{fd}$ . We consider the

This is the author's peer reviewed, accepted manuscript. However, the online version of record will be different from this version once it has been copyedited and typeset.

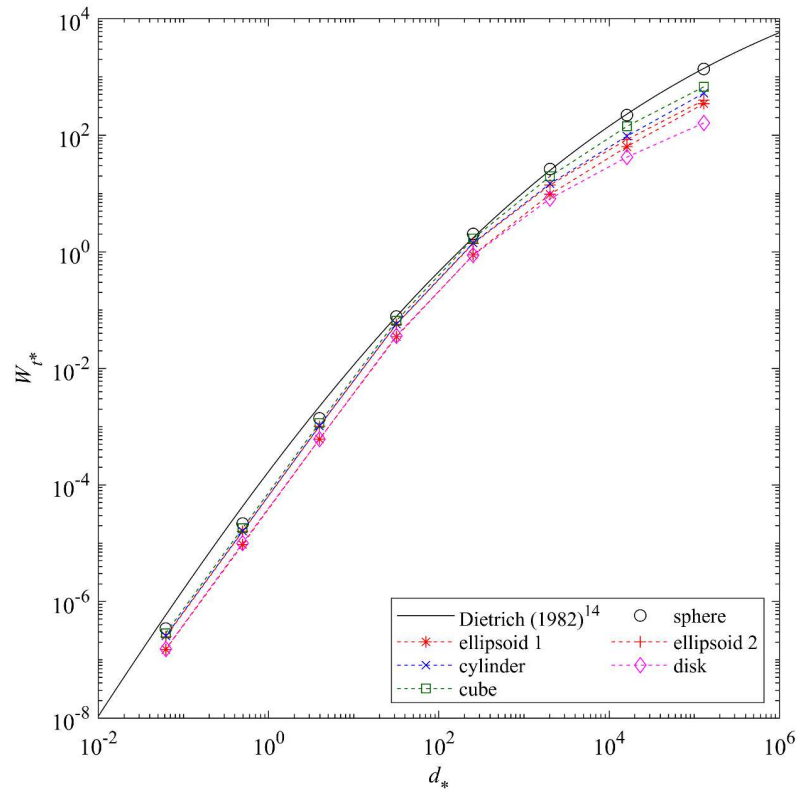
PLEASE CITE THIS ARTICLE AS DOI: 10.1063/5.0165555

Accepted to *Phys. Fluids* 10.1063/5.0165555

259 drag ratio  $F_{fd} / F_{pd}$  which is defined as the ratio between friction drag and pressure drag  
 260 of a particle at the terminal settling state. Figure 4 illustrates the dependency of the drag  
 261 ratio  $F_{fd} / F_{pd}$  on particle Reynolds number  $Re_p$ . The computed  $F_{fd} / F_{pd}$  of spheres  
 262 settling in the Stokes regime is approximately 2, close to the theoretically derived value.<sup>2</sup>  
 263 Moreover, the computed  $F_{fd} / F_{pd}$  of a specific shape remains constant throughout the  
 264 Stokes regime and gradually decreases as  $Re_p$  increases in the intermediate regime. For  
 265 given  $Re_p$ , the value of  $F_{fd} / F_{pd}$  generally increases with increasing CSF. These  
 266 results suggest that when the inertial force becomes significant or the particle shape  
 267 deviates from spherical, pressure drag gradually dominates over friction drag.  
 268

This is the author's peer reviewed, accepted manuscript. However, the online version of record will be different from this version once it has been copyedited and typeset.  
 PLEASE CITE THIS ARTICLE AS DOI: 10.1063/5.0165555

Accepted to Phys. Fluids 10.1063/5.0165555



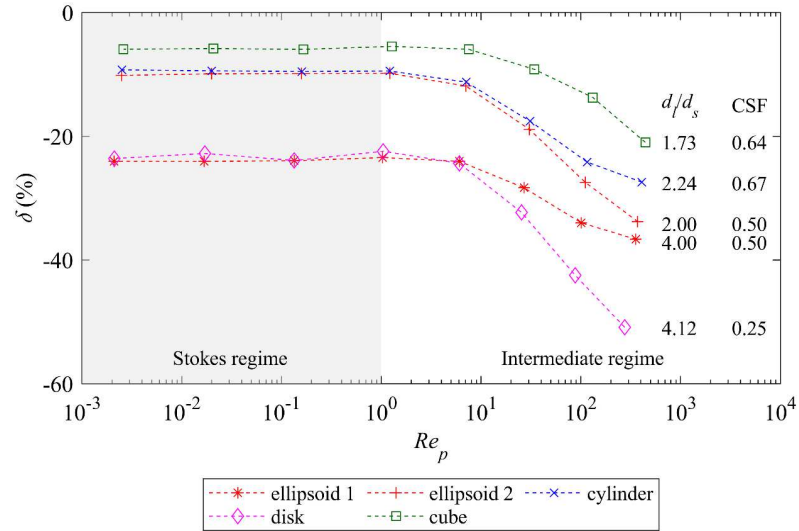
269

270 **FIG. 1.** Dimensionless terminal velocity  $W_{t*}$  against dimensionless spherical equivalent  
 271 diameter  $d_*$  obtained for different particle shapes when  $\beta_0 = 0^\circ$ . Solid line refers to the  
 272 model by Dietrich<sup>14</sup>.

273

This is the author's peer reviewed, accepted manuscript. However, the online version of record will be different from this version once it has been copyedited and typeset.  
 PLEASE CITE THIS ARTICLE AS DOI: 10.1063/5.0165555

Accepted to Phys. Fluids 10.1063/5.0165555



274

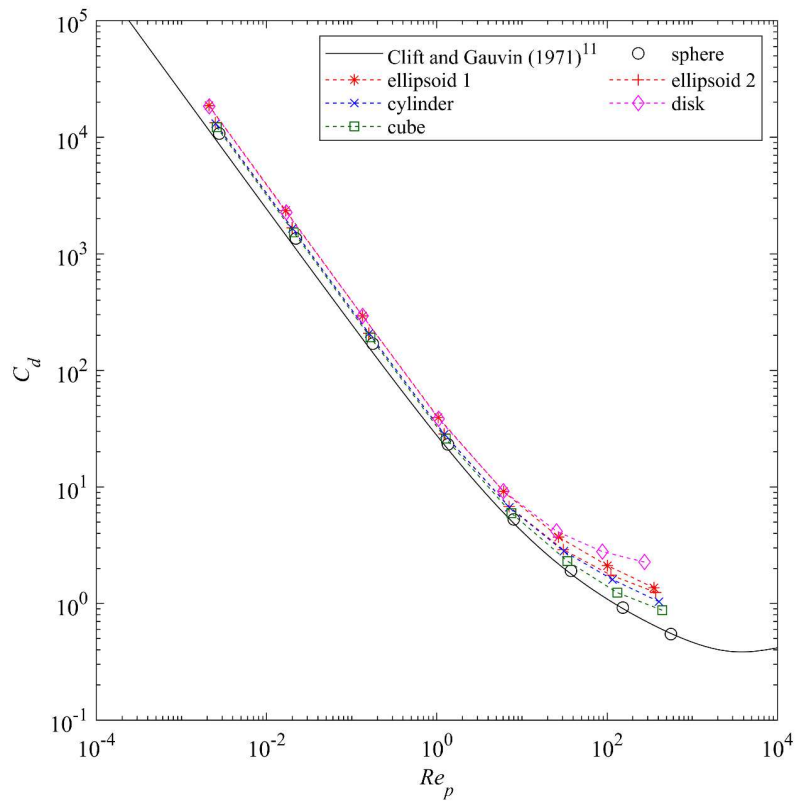
275 **FIG. 2.** Predicted dependence of relative deviation  $\delta$  in terminal velocity of a non-  
 276 spherical particle to that of a sphere of the same equivalent diameter on particle Reynolds  
 277 number  $Re_p$ .

278



This is the author's peer reviewed, accepted manuscript. However, the online version of record will be different from this version once it has been copyedited and typeset.  
 PLEASE CITE THIS ARTICLE AS DOI: 10.1063/5.0165555

Accepted to Phys. Fluids 10.1063/5.0165555



279

280 **FIG. 3.** Dependence of predicted drag coefficient  $C_d$  on particle Reynolds number  $Re_p$ .

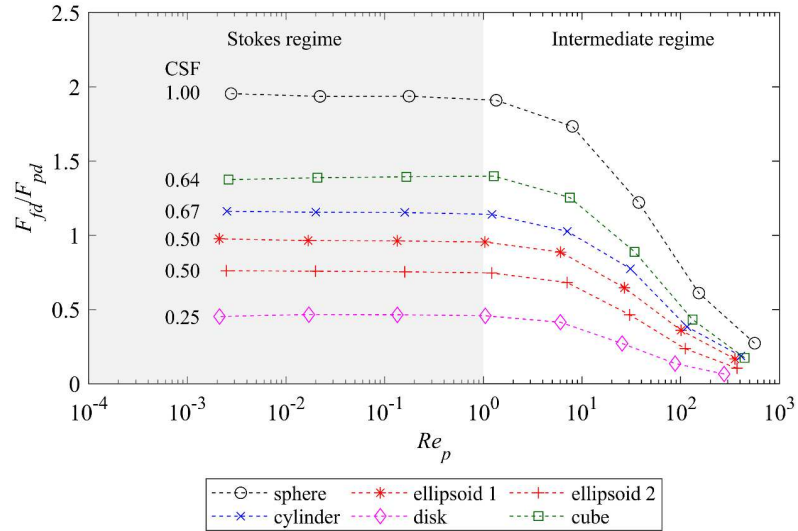
281 Solid line is the spherical drag law proposed by Clift and Gauvin<sup>11</sup>.

282

283

This is the author's peer reviewed, accepted manuscript. However, the online version of record will be different from this version once it has been copyedited and typeset.  
 PLEASE CITE THIS ARTICLE AS DOI: 10.1063/5.0165555

Accepted to Phys. Fluids 10.1063/5.0165555



284

285 **FIG. 4.** Predicted dependence of drag ratio  $F_{fd} / F_{pd}$  on particle Reynolds number  $Re_p$ .

286

287 2. *Characteristic time and displacement*

288 Although the settling velocity and drag coefficient have been extensively studied for  
289 both spherical and non-spherical particles, limited attention has been paid to the time and  
290 space scales required for a particle to reach its terminal settling state.

291 The motion of a spherical particle falling through a fluid is described theoretically  
292 by the Boussinesq-Basset-Oseen equation,<sup>2</sup> expressed as

$$293 \quad (m_p + \alpha_m m_f) \frac{dW}{dt} = (m_p - m_f)g - F_d - \frac{3}{2} d_n^2 (\pi \rho_f \mu)^{1/2} \int_0^t \frac{dW}{d\sigma} \frac{d\sigma}{(t - \sigma)^{1/2}}, \quad (12)$$

294 where  $m_f$  is the mass of fluid displaced by the sphere;  $\alpha_m$  is the added mass  
295 coefficient; and  $\sigma$  is a dummy variable. In Eq. (12), the term on the left-hand side  
296 denotes particle inertia, and includes the added mass effect when an accelerating (or  
297 retarding) particle moves in a fluid. In practice, it is common to assume  $\alpha_m = 0.5$ . On  
298 the right-hand side of Eq. (12), the first term is the submerged weight of the particle, the  
299 second term represents the fluid drag, and the third term is the Basset force (due to particle  
300 acceleration because of unsteady viscous shear on the surface of the particle).

301 Guo<sup>44</sup> derived a simple closed-form solution for the motion of a sphere settling  
302 through a fluid by applying Rubey's drag law<sup>45</sup> to Eq. (12) and combining the added mass  
303 and the Basset force into an integrated term. Guo was able to determine analytically the  
304 time-dependent settling velocity, acceleration, and vertical displacement of a spherical  
305 particle. However, for a non-spherical particle, even when the orientation variation is  
306 neglected and the drag force approximated by an empirical relationship, it is extremely  
307 difficult to obtain analytical solutions for the added mass and the Basset force. In practice,  
308 empirical relations have to be introduced in order to describe the characteristic time and  
309 characteristic displacement of a settling non-spherical particle.

310 Here, we focus on cases with  $\beta_0 = 0^\circ$ , where particles accelerate to the terminal  
 311 settling state with negligible change in orientation. The characteristic time  $t_{95}$  and  
 312 characteristic displacement  $s_{95}$  are defined as the time and vertical displacement taken  
 313 for a particle to reach 95% of its terminal velocity. A general dimensional analysis gives  
 314 the following expressions:

$$315 \quad t_{95*} = \frac{t_{95}}{d_n^2 / \nu} = f_1(Re_p), \quad (13)$$

$$316 \quad s_{95*} = \frac{s_{95}}{d_n} = f_2(Re_p), \quad (14)$$

317 where  $t_{95*}$  and  $s_{95*}$  are dimensionless characteristic time and displacement. Figure 5  
 318 depicts the behavior of  $t_{95*}$  and  $s_{95*}$  with  $Re_p$ , as logarithmic plots. Linear fitting is  
 319 used to obtain two asymptotes for the Stokes and intermediate regimes, with their  
 320 intersection set at  $Re_p = 1$ . As shown in Fig. 5(a), the dimensionless characteristic time  
 321  $t_{95*}$  is assumed constant throughout much of the Stokes regime, and then decreases with  
 322 increasing  $Re_p$  in the intermediate regime. The dimensionless characteristic  
 323 displacement  $s_{95*}$  increases monotonically with increasing  $Re_p$  over the simulated  
 324 range, with the linear slope observed in the Stokes regime reducing in the intermediate  
 325 regime [Fig. 5(b)]. These results suggest that the Stokes and intermediate regimes are  
 326 characterized by two distinct acceleration mechanisms. Based on the two asymptotes, the  
 327 logarithmic matching approach proposed by Guo<sup>46</sup> is used to establish the following  
 328 correlation formulae:

$$329 \quad t_{95*} = 2.226 \left(1 + Re_p^{3.126}\right)^{-0.222}, \quad (15)$$

$$330 \quad s_{95*} = 1.716 Re_p^{0.998} \left(1 + Re_p^{3.409}\right)^{-0.209}. \quad (16)$$

This is the author's peer reviewed, accepted manuscript. However, the online version of record will be different from this version once it has been copyedited and typeset.

PLEASE CITE THIS ARTICLE AS DOI: 10.1063/5.0165555

*Accepted to Phys. Fluids 10.1063/5.0165555*

331 The above correlations are evaluated using the coefficient of determination  $R^2$  and  
 332 mean relative error MRE, which are defined as

$$333 \quad R^2 = 1 - \frac{\sum_{k=1}^N (\eta_k^{\text{cal}} - \eta_k^{\text{sim}})^2}{\sum_{k=1}^N (\overline{\eta^{\text{sim}}} - \eta_k^{\text{sim}})^2}, \quad (17)$$

$$334 \quad \text{MRE} = \frac{1}{N} \sum_{k=1}^N \left| \frac{\eta_k^{\text{cal}} - \eta_k^{\text{sim}}}{\eta_k^{\text{sim}}} \right|, \quad (18)$$

335 where  $\eta_k^{\text{cal}}$  is the  $k$ -th data value obtained from the correlation functions;  $\eta_k^{\text{sim}}$  is the  $k$ -  
 336 th data value from the numerical simulations;  $\overline{\eta^{\text{sim}}}$  is the mean value of the simulated  
 337 data; and  $N$  is the number of pairs of data points. In general, higher  $R^2$  and lower  
 338 MRE correspond to better model performance. As demonstrated in Table III, our  
 339 theoretical model exhibits rather good performance with high  $R^2$  and acceptable MRE.  
 340 The proposed correlations indicate that the time and space scales required for a non-  
 341 spherical particle to reach its terminal settling state may vary with  $Re_p$ , and provide  
 342 convenient methods that give effective estimates of the magnitudes of the characteristic  
 343 time and displacement. It should be noted that the proposed correlations are only valid  
 344 within the simulated range of  $Re_p$  for a particle-to-fluid density ratio  $\rho_p / \rho_f$  of 2.65.  
 345 Future work will be extended to the Newton regime ( $Re_p > 10^3$ ) and incorporate a larger  
 346 range of density ratios.

347

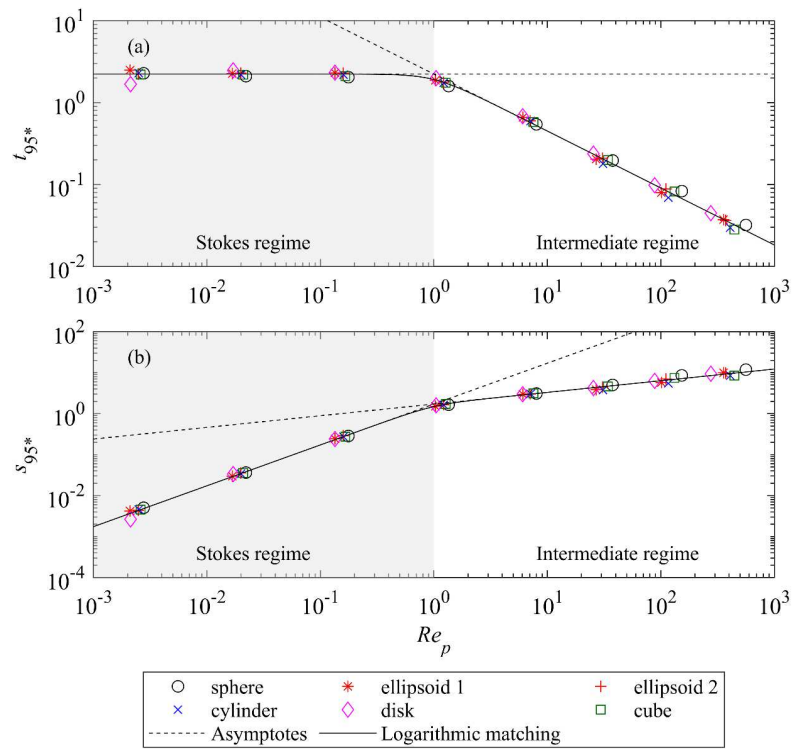
This is the author's peer reviewed, accepted manuscript. However, the online version of record will be different from this version once it has been copyedited and typeset.  
 PLEASE CITE THIS ARTICLE AS DOI: 10.1063/5.0165555

Accepted to Phys. Fluids 10.1063/5.0165555

348 **TABLE III.** Performance of proposed correlation formulae Eq. (15) for dimensionless  
 349 characteristic time and Eq. (16) for dimensionless characteristic displacement against  
 350 underlying simulated data.

Correlation	$R^2$	MRE (%)
Eq. (15)	0.9971	5.948
Eq. (16)	0.9988	3.453

351



352

353 **FIG. 5.** Dependence on particle Reynolds number  $Re_p$  of (a) dimensionless  
 354 characteristic time  $t_{95^*}$  and (b) dimensionless characteristic displacement  $s_{95^*}$ .

355

## 356 B. Particle settling with different initial orientations

## 357 1. Stokes regime

358 In this section, results from numerical cases with  $d_n = 0.0625$  mm and  $Re_p$   
 359 ranging from 0.1 to 0.2 are analyzed to investigate the effect of initial orientation on the  
 360 settling of non-spherical particles in the Stokes regime. Note that similar results are found  
 361 for cases with  $d_n = 0.015625$  mm and  $2 \times 10^{-3} < Re_p < 3 \times 10^{-3}$ , and so are not included  
 362 here.

363 Taking ellipsoid 1 as an example, Figure 6 shows the temporal variations in  
 364 orientation angle  $\beta$ , settling velocity  $W$ , and vertical displacement  $s$ . It can be seen  
 365 that  $\beta$  remains constant during the settling process for cases with different  $\beta_0$  [Fig.  
 366 6(a)]. This suggests that the orientation remains essentially unchanged for non-spherical  
 367 particles settling in the Stokes regime, in agreement with previous findings.<sup>27,28</sup> As a result,  
 368 a non-spherical particle reaches a terminal velocity that depends on the initial orientation  
 369 of the particle [Fig. 6(b)]. And particles with larger  $\beta_0$  tend to settle faster, yielding  
 370 longer vertical displacements [Fig. 6(c)].

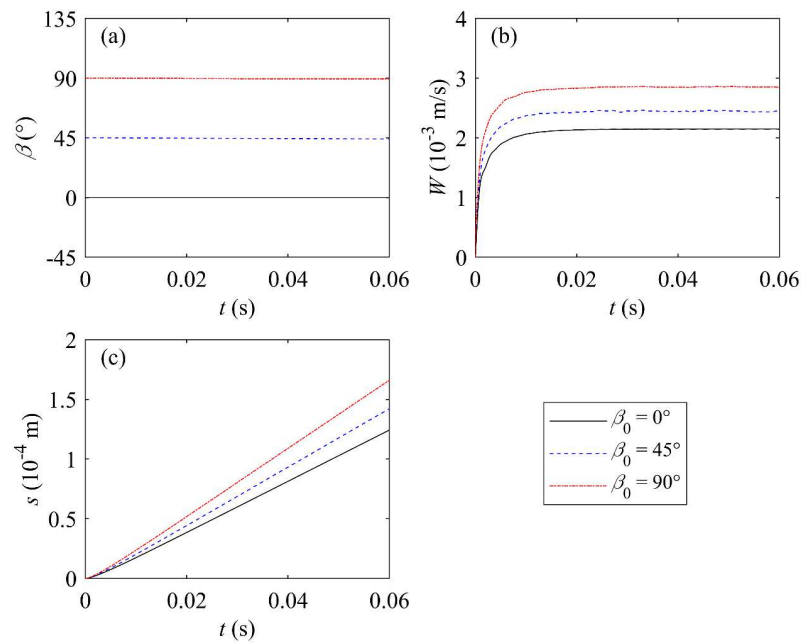
371 To account for the effect of particle orientation, we consider crosswise sphericity  
 372  $\phi_c$ , which is the ratio between the cross-sectional area of a volume-equivalent sphere and  
 373 the projection area of the actual particle perpendicular to the flow.<sup>16</sup> According to the  
 374 definition of  $\beta$ , particles with large  $\beta$  should have relatively small projection areas  
 375 and consequently develop large  $\phi_c$ .

376 Figure 7 illustrates the influence of particle orientation on terminal settling state by  
 377 showing the resulting variations in terminal velocity  $W_t$  and drag ratio  $F_{fd} / F_{pd}$  with  
 378  $\phi_c$ . In general, larger  $\phi_c$  leads to larger  $W_t$ , indicating that the particle experiences

This is the author's peer reviewed, accepted manuscript. However, the online version of record will be different from this version once it has been copyedited and typeset.  
 PLEASE CITE THIS ARTICLE AS DOI: 10.1063/5.0165555

Accepted to Phys. Fluids 10.1063/5.0165555

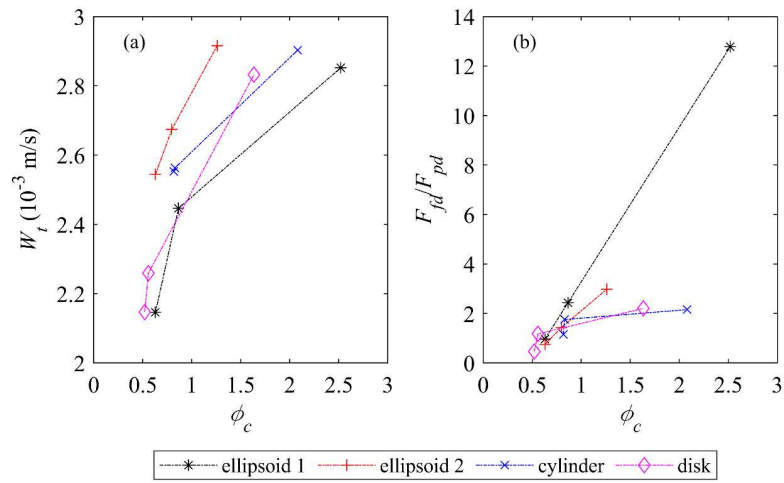
379 lower total drag at larger  $\beta$ . In addition,  $F_{fd} / F_{pd}$  tends to increase as  $\phi_c$  increases,  
 380 implying that the contribution from friction drag may increase despite reduction in total  
 381 drag when the particle is oriented away from  $\beta = 0^\circ$ . Figure 8 presents contour plots of  
 382 vertical flow velocity in the vicinity of particles of different shapes and initial orientation  
 383  $\beta_0 = 45^\circ$  at the terminal settling state. Cases with  $\beta_0 = 45^\circ$  are of particular interest  
 384 because the particles display asymmetric forms in the vertical plane. As shown in Fig. 8,  
 385 the velocity contours exhibit a highly symmetric pattern and turn out to be similar for  
 386 different particle shapes. The particles seem to move in combination with the surrounding  
 387 fluid, and so the effect of asymmetry of the solid shape is marginal. Arguably, this  
 388 accounts for the sustainability of random orientations.



389  
 390 **FIG. 6.** Time histories of (a) orientation angle  $\beta$ , (b) settling velocity  $W$ , and (c)



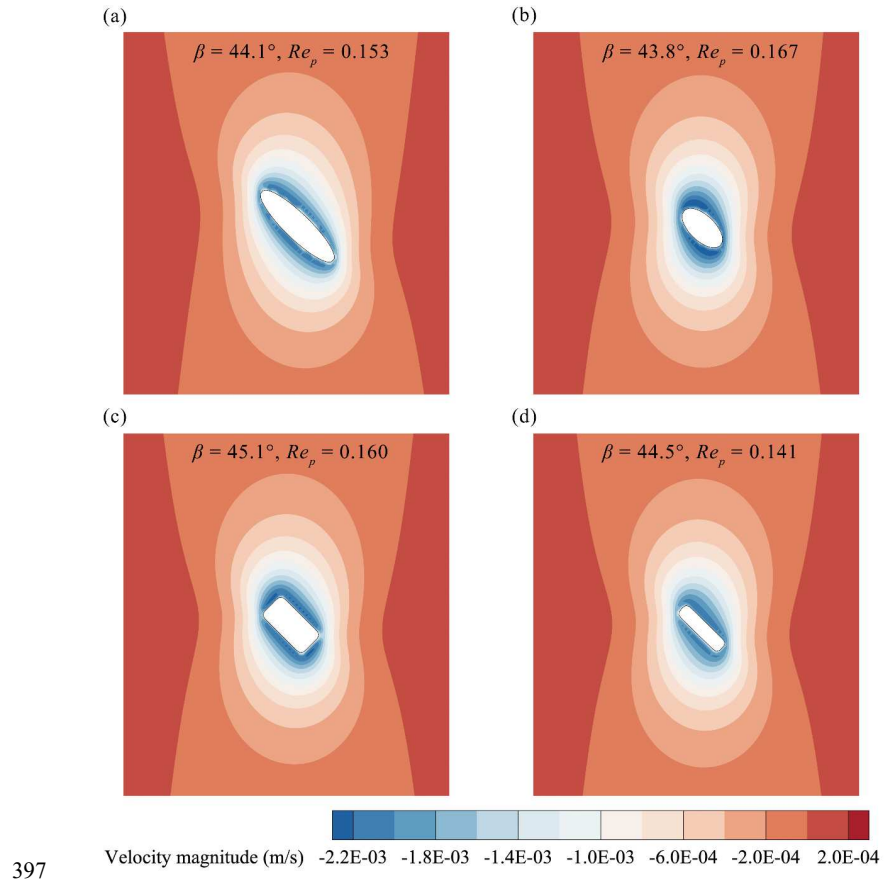
391 vertical displacement  $s$  for ellipsoid 1 with  $d_n = 0.0625$  mm.  
392



393  
394 **FIG. 7.** Predicted dependencies of (a) terminal velocity  $W_t$  and (b) drag ratio  $F_{fd} / F_{pd}$   
395 on crosswise sphericity  $\phi_c$  for particles of different shapes with  $d_n = 0.0625$  mm.  
396

This is the author's peer reviewed, accepted manuscript. However, the online version of record will be different from this version once it has been copyedited and typeset.  
 PLEASE CITE THIS ARTICLE AS DOI: 10.1063/5.0165555

Accepted to Phys. Fluids 10.1063/5.0165555



397

398 **FIG. 8.** Contour plots of vertical flow velocity component around differently shaped  
 399 particles with  $d_n = 0.0625$  mm and  $\beta_0 = 45^\circ$  at the terminal settling state ( $t = 0.06$  s):  
 400 (a) ellipsoid 1, (b) ellipsoid 2, (c) cylinder, and (d) disk.

401

402 2. *Intermediate regime*

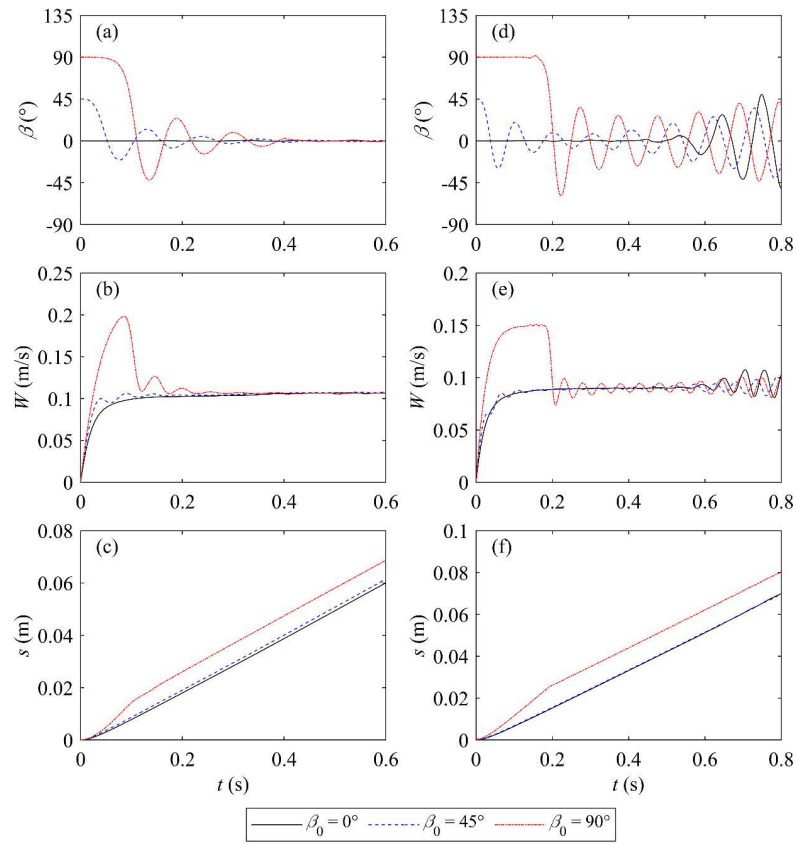
403 Here numerical cases with  $d_n = 1$  mm and  $Re_p \approx 100$  are selected to probe into  
 404 the effect of initial orientation on the settling of non-spherical particles in the intermediate  
 405 regime. As can be seen from Fig. 9(a), particles of ellipsoid 1 shape tend to attain the  
 406 same terminal settling state with  $\beta = 0^\circ$  irrespective of their initial orientation,  
 407 consistent with the previously mentioned settling behavior at relatively large  $Re_p$ .<sup>8,29</sup>  
 408 Variation in particle orientation has a vital effect on the settling process, about which more  
 409 details are given later in this section. Yet, due to the identical orientation attained at  
 410 terminal settling, the effect of initial orientation on terminal velocity can be negligible  
 411 [see Fig. 9(b)]. Except for the disk, similar results have been found for other particle  
 412 shapes. At the terminal settling state, periodic oscillations about  $\beta = 0^\circ$  are observed for  
 413 the disk particle [Figs. 9(d) and 9(e)]. Such results are in accordance with previous  
 414 observations by Stringham et al.<sup>47</sup> at a higher value of  $Re_p$ .

415 Figure 10 depicts two-dimensional visualizations of the settling trajectory and  
 416 orientation variation of different particles with  $\beta_0 = 90^\circ$ . The red dashed line denotes the  
 417 centroid trajectory and the black solid line with blue endpoints denotes the location of the  
 418 revolution axis. The time increment between each visualization is 0.02 s. During the  
 419 settling process, the revolution axes of elongated particles (ellipsoid 1 and the cylinder)  
 420 become gradually oriented normal to the direction of settling motion, while those of flat  
 421 particles (ellipsoid 2 and the disk) turn to be parallel to the settling direction, thus the  
 422  $\beta = 0^\circ$  state is eventually reached. In addition to the vertical fall, a horizontal component  
 423 can be observed in the settling path, associated with the varying orientation.

424

This is the author's peer reviewed, accepted manuscript. However, the online version of record will be different from this version once it has been copyedited and typeset.  
PLEASE CITE THIS ARTICLE AS DOI: 10.1063/5.0165555

Accepted to Phys. Fluids 10.1063/5.0165555



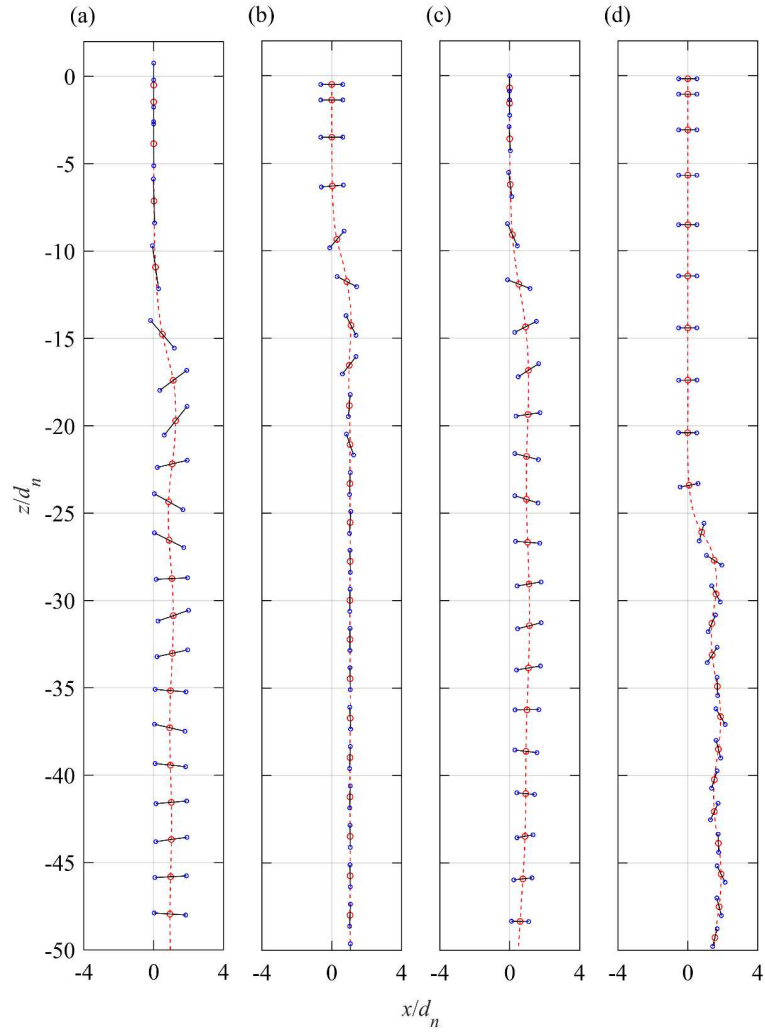
425

426 **FIG. 9.** Time histories of orientation angle  $\beta$ , settling velocity  $W$ , and vertical  
427 displacement  $s$  for (a-c) ellipsoid 1 and (d-f) disk with  $d_n = 1$  mm.

428

This is the author's peer reviewed, accepted manuscript. However, the online version of record will be different from this version once it has been copyedited and typeset.  
 PLEASE CITE THIS ARTICLE AS DOI: 10.1063/5.0165555

Accepted to Phys. Fluids 10.1063/5.0165555



429

430 **FIG. 10.** Variations in settling trajectory and orientation of different particles with  
 431  $d_n = 1$  mm,  $\beta_0 = 90^\circ$  and shape: (a) ellipsoid 1, (b) ellipsoid 2, (c) cylinder, and (d) disk.  
 432 Red dashed line denotes the centroid trajectory, and black solid line with blue endpoints  
 433 denotes the location of the revolution axis. The lengths of the revolution axes of ellipsoid  
 434 2 and the disk are doubled and tripled respectively for clarity. The time increment between  
 435 each visualization is 0.02 s.

436           Given that gravitational force induces no torque about the mass center, torque arising  
 437 from hydrodynamic forces is responsible for particle rotation. According to Mandø and  
 438 Rosendahl<sup>8</sup>, friction torque always acts to damp rotational motion, whereas torque  
 439 stemming from the offset of the center of pressure from the geometric center (i.e., the  
 440 mass center) accounts for orientation readjustment of the particle. Figure 11 illustrates the  
 441 pressure distribution around ellipsoid 1 at different instants of settling with  $\beta_0 = 90^\circ$ .  
 442 During the initial period, the particle moves at its initial orientation (i.e.,  $\beta = \beta_0 = 90^\circ$ )  
 443 [Fig. 11(a)]. Although the particle experiences no torque under such circumstances, this  
 444 can instinctively be interpreted as a state of unstable equilibrium. Once it experiences a  
 445 certain level of disturbance, the particle starts to deviate from the state of unstable  
 446 equilibrium, and the pressure distribution is no longer symmetric around the particle [Figs.  
 447 11(b) and 11(c)]. This change promotes additional torque due to the displacement of the  
 448 center of pressure, thus forcing the particle to rotate. Eventually, a state of stable  
 449 equilibrium is reached whereby the center of pressure is consistent with the geometric  
 450 center, and the torque vanishes [Fig. 11(d)]. The terminal settling state of a particle is  
 451 commonly characterized by this stable equilibrium state without regard to secondary  
 452 motions like oscillation.

453           Based on the above description, the settling process of a non-spherical particle in the  
 454 intermediate regime may be divided into three chronological stages. In Stage 1, the  
 455 particle provisionally settles at an unstable equilibrium state. In Stage 2, the particle self-  
 456 readjusts to a stable equilibrium state. In Stage 3, the particle progressively attains the  
 457 terminal settling state where secondary motions may occur. Notably, particles with certain  
 458 initial orientations may not experience Stage 1 and even Stage 2. Moreover, the settling  
 459 velocity can dramatically increase in Stage 1, leading to a considerably longer vertical

460 displacement [see Figs. 9(c) and 9(f)]. Particles with  $d_n = 0.25$  mm ( $Re_p \approx 10$ ) exhibit  
 461 qualitatively similar settling behavior to those with  $d_n = 1$  mm, yet appear to be oriented  
 462 directly to the stable equilibrium state of  $\beta = 0^\circ$  without exhibiting oscillations in Stage  
 463 2 (Fig. 12).

464 As a settling particle rotates due to hydrodynamic torque, the rotational motion of  
 465 the particle can in turn appreciably affect its local flow field, leading to specific wake  
 466 structures. Figure 13 visualizes the flow fields around particles of different shapes with  
 467  $d_n = 1$  mm and  $\beta_0 = 90^\circ$ . The  $\Omega_R$  method proposed by Dong et al.<sup>48</sup> is used for vortex  
 468 identification. An iso-surface of  $\Omega_R = 0.52$  is chosen to capture the vortical structures.  
 469 As illustrated in Fig. 13(a), the wake of ellipsoid 1 initially consists of two thread-like  
 470 vortices that are attached to the particle. As the particle rotates, instability develops, and  
 471 vortex shedding occurs. The detached vortices push the flow near and around the particle  
 472 upwards, forming a low-pressure region that generates a torque on the particle in the  
 473 opposite direction. This additional torque along with inertia can further lead to particle  
 474 oscillations because new vortices can detach on the other side when the particle reaches  
 475 the opposite inclination and so on, each time the particle changes orientation. Notably,  
 476 the vortical structure is closely related to the particle shape. Similar to ellipsoid 1, a  
 477 double-threaded wake structure is observed for the cylinder [Fig. 13(c)], whereas flatter  
 478 particles like ellipsoid 2 and the disk present a so-called hairpin structure<sup>49,50</sup> [Figs. 13(b)  
 479 and 13(d)]. Vortex shedding is less pronounced for particles with  $d_n = 1$  mm and  
 480  $\beta_0 = 45^\circ$ . This is mainly because the absence of Stage 1 leads to relatively low  $Re_p$  in  
 481 Stage 2. For particles with  $d_n = 0.25$  mm however, no vortex shedding is observed for  
 482 all simulated shapes and initial orientations. The foregoing suggests that the occurrence

This is the author's peer reviewed, accepted manuscript. However, the online version of record will be different from this version once it has been copyedited and typeset.

PLEASE CITE THIS ARTICLE AS DOI: 10.1063/5.0165555

Accepted to *Phys. Fluids* 10.1063/5.0165555

483 of vortex shedding depends largely on the magnitude of  $Re_p$ . An unstable initial  
484 orientation may promote vortex shedding because larger  $Re_p$  can be reached and  
485 rotational motion is induced. In turn, vortex shedding can affect the settling motion by  
486 causing the particle to oscillate in Stage 2 and Stage 3.

487 Figure 14 presents contour plots of the vertical flow velocity component around  
488 particles of different shapes with  $d_n = 1$  mm and  $\beta_0 = 90^\circ$ . Sinuous wake structures  
489 associated with varying particle orientation can be observed. Moreover, the velocity  
490 distribution in the wake exhibits an asymmetric pattern even as the particle approaches  
491 the state of stable equilibrium [Figs. 14(a) and 14(d)]. In fact, the high-velocity zone is  
492 located close to the downward-rotating end of the particle, reflecting the effect of  
493 rotational motion on the flow field.

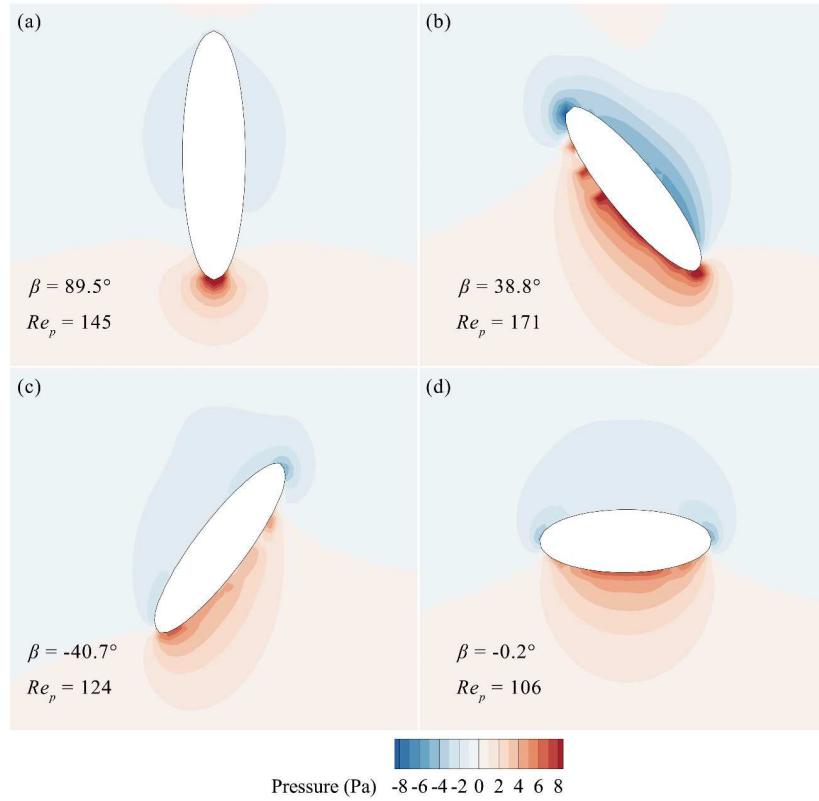
494 Overall, our results provide insight into the settling process of non-spherical particles  
495 in the intermediate regime. The initial orientation of non-spherical particles plays a key  
496 role in the settling process and so should be taken into account for particulate flows.

497



This is the author's peer reviewed, accepted manuscript. However, the online version of record will be different from this version once it has been copyedited and typeset.  
 PLEASE CITE THIS ARTICLE AS DOI: 10.1063/5.0165555

Accepted to Phys. Fluids 10.1063/5.0165555



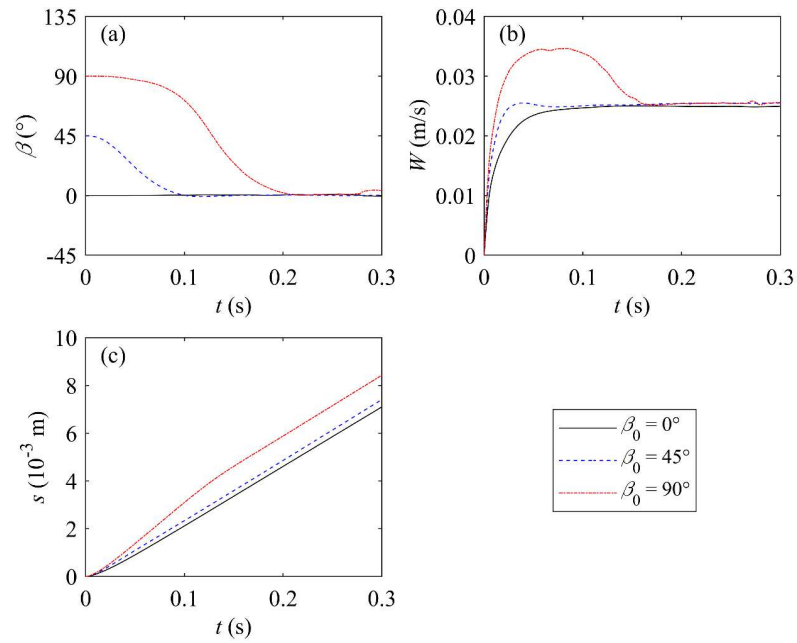
498

499 **FIG. 11.** Pressure distribution contours around ellipsoid 1 with  $d_n = 1$  mm and  
 500  $\beta_0 = 90^\circ$  at different instants of settling:  $t =$  (a) 0.04 s, (b) 0.10 s, (c) 0.14 s, and (d)  
 501 0.60 s.

502

This is the author's peer reviewed, accepted manuscript. However, the online version of record will be different from this version once it has been copyedited and typeset.  
PLEASE CITE THIS ARTICLE AS DOI: 10.1063/5.0165555

Accepted to Phys. Fluids 10.1063/5.0165555



503

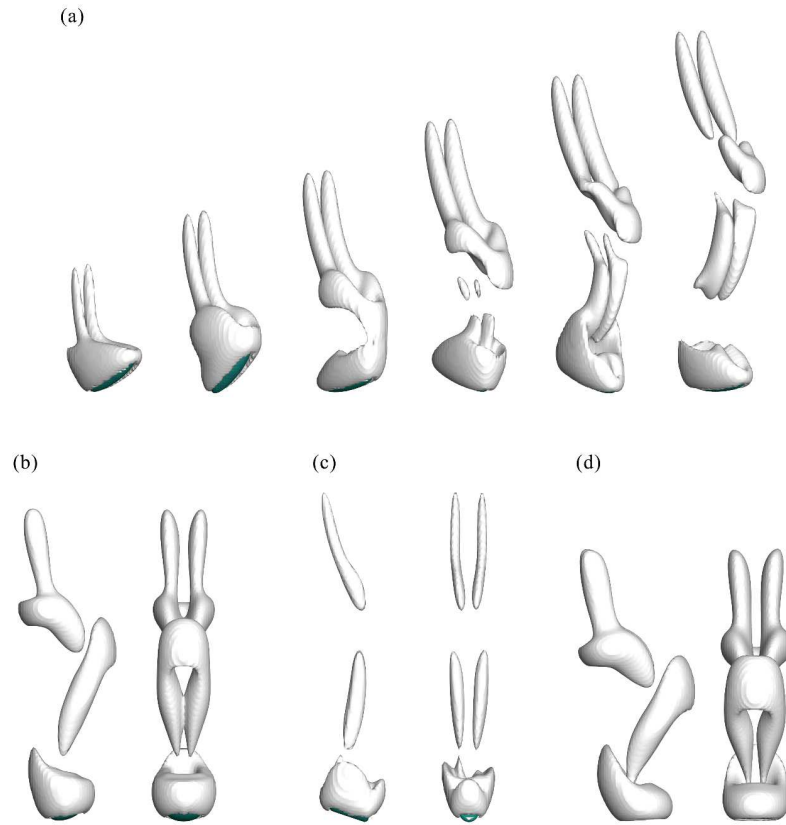
504 **FIG. 12.** Time histories of (a) orientation angle  $\beta$ , (b) settling velocity  $W$ , and (c)

505 vertical displacement  $s$  for ellipsoid 1 with  $d_n = 0.25$  mm.

506

This is the author's peer reviewed, accepted manuscript. However, the online version of record will be different from this version once it has been copyedited and typeset.  
PLEASE CITE THIS ARTICLE AS DOI: 10.1063/5.0165555

Accepted to Phys. Fluids 10.1063/5.0165555



507

508 **FIG. 13.** Vortices in the wake of particles of different shapes with  $d_p = 1$  mm and

509  $\beta_0 = 90^\circ$  during orientation readjustment: (a) ellipsoid 1,  $t = 0.12\text{--}0.22$  s, (b) ellipsoid 2,

510  $t = 0.18$  s, (c) cylinder,  $t = 0.20$  s, and (d) disk,  $t = 0.30$  s. An iso-surface of  $\Omega_R = 0.52$

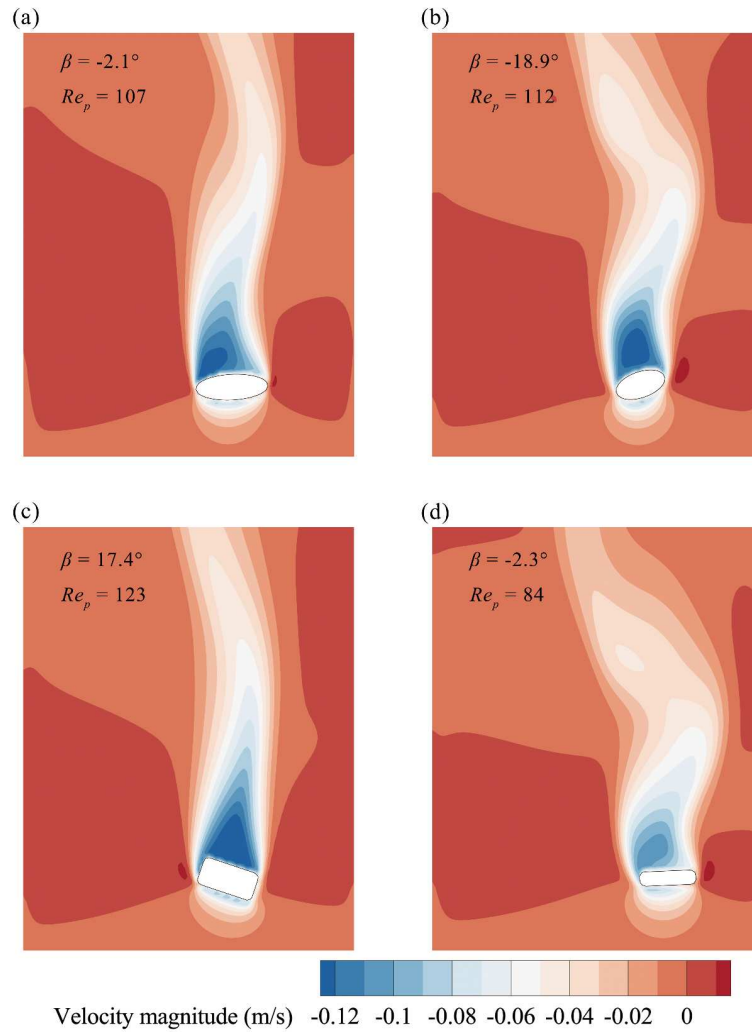
511 is chosen to capture vortical structures.<sup>48</sup>

512

This is the author's peer reviewed, accepted manuscript. However, the online version of record will be different from this version once it has been copyedited and typeset.

PLEASE CITE THIS ARTICLE AS DOI: 10.1063/5.0165555

Accepted to Phys. Fluids 10.1063/5.0165555



513

514 **FIG. 14.** Contour plots of vertical flow velocity component around particles of different  
 515 shapes with  $d_n = 1$  mm and  $\beta_0 = 90^\circ$  during orientation readjustment: (a) ellipsoid 1,  
 516  $t = 0.22$  s, (b) ellipsoid 2,  $t = 0.18$  s, (c) cylinder,  $t = 0.20$  s, and (d) disk,  $t = 0.30$  s.

517

518 IV. CONCLUSION

519 This study has investigated the effects of particle shape and initial orientation on the  
 520 settling of non-spherical particles. Commercial CFD software FLOW-3D was used to  
 521 perform a series of PR-DNS simulations of the settling in otherwise quiescent water of  
 522 spheres and five types of regular, non-spherical sediment particles, i.e., prolate spheroid,  
 523 oblate spheroid, cylinder, disk, and cube. A dual-Euler whole-attitude solver was used to  
 524 reproduce particle orientation behavior. In the study, the Galileo number was varied from  
 525 0.248 to 360 with the particle Reynolds number  $Re_p$  ranging from 0.00277 to 562.

526 Based on the computational results, the main findings are summarized as follows:

527 (1) A non-spherical particle experiences larger drag and consequently attains a lower  
 528 terminal velocity than its spherical counterpart. For sufficiently small  $Re_p$ ,  
 529 when the viscous force dominates, the terminal velocity is less affected by the  
 530 particle shape (characterized by the particle aspect ratio). For relatively large  
 531  $Re_p$  when the inertial force becomes dominant, the shape effect becomes  
 532 significant, and should be represented by the Corey shape factor. When the  
 533 inertial force becomes significant or the particle shape deviates from a sphere,  
 534 then pressure drag may dominate over friction drag.

535 (2) Empirical correlations were derived for the dimensionless characteristic time  
 536  $t_{95^*}$  and dimensionless characteristic displacement  $s_{95^*}$  of particle settling. It  
 537 was demonstrated that  $t_{95^*}$  remains constant in the Stokes regime and decreases  
 538 as  $Re_p$  increases in the intermediate regime;  $s_{95^*}$  increases logarithmically  
 539 with increasing  $Re_p$  over the simulated range, whereas the slope in  $s_{95^*}$  with  
 540  $Re_p$  observed in the Stokes regime reduces in the intermediate regime.

541 (3) In the Stokes regime, the orientation of a non-spherical particle remains  
 542 essentially unchanged during the settling process. A non-spherical particle with  
 543 different initial orientations can attain various terminal velocities which increase  
 544 with crosswise sphericity  $\phi_c$ . The flow velocity distribution in the vicinity of a  
 545 particle of any shape exhibits a highly symmetric pattern. A given particle  
 546 appears to move in tandem with the surrounding fluid, such that the effect of its  
 547 asymmetry is marginal.

548 (4) In the intermediate regime, a non-spherical particle provisionally settling at an  
 549 unstable orientation tends to readjust itself to a stable equilibrium state. In  
 550 general, such a particle may experience three stages during its settling process:  
 551 settling provisionally at an unstable equilibrium state; self-readjusting to a stable  
 552 equilibrium state; and progressively approaching the terminal state where  
 553 secondary motions may occur. Due to the identical orientation attained at  
 554 terminal settling, the effect of initial orientation on terminal velocity is negligible,  
 555 while an unstable initial orientation can result in a longer vertical displacement  
 556 and may promote vortex shedding. It is therefore important to consider the initial  
 557 orientation of non-spherical particles when modeling particulate flows.

558 In many real-world situations, particles do not settle in isolation. Vortices induced by  
 559 nearby particles can significantly influence the overall settling behavior, e.g., causing  
 560 repulsion in dual-particle cases,<sup>51</sup> promoting clusters for monodisperse particles,<sup>52</sup> and  
 561 altering the orientation of rod-like particles.<sup>53</sup> Direct inter-particle interactions (collisions)  
 562 also play an important role in the dynamics of particles particularly when in a dense  
 563 regime.<sup>54,55</sup> Therefore, we intend to carry out future research into the behavior of multi-  
 564 particle systems. Moreover, the present work has provided us with a unique basis to  
 565 further investigate the settling of irregular particles; this work is underway.

This is the author's peer reviewed, accepted manuscript. However, the online version of record will be different from this version once it has been copyedited and typeset.

PLEASE CITE THIS ARTICLE AS DOI: 10.1063/5.0165555

*Accepted to Phys. Fluids 10.1063/5.0165555*

566

## 567 SUPPLEMENTARY MATERIAL

568 The Supplementary Material provides a brief description of the dual-Euler whole-  
569 attitude solver used to model variation in particle orientation.

570

## 571 ACKNOWLEDGMENTS

572 The present work was financially supported by the National Natural Science  
573 Foundation of China (Grant No. 52239007).

574

## 575 AUTHOR DECLARATIONS

### 576 Conflict of Interest

577 The authors have no conflicts to disclose.

578

### 579 Author Contributions

580 **Xiaoyong Cheng:** Data curation (lead); Formal analysis (lead); Investigation (equal);  
581 Methodology (equal); Validation (lead); Visualization (lead); Writing – original draft  
582 (lead). **Zhixian Cao:** Conceptualization (equal); Funding acquisition (lead); Investigation  
583 (equal); Methodology (equal); Project administration (lead); Resources (lead);  
584 Supervision (lead); Writing – review & editing (equal). **Ji Li:** Conceptualization (equal);  
585 Investigation (equal); Writing – review & editing (equal). **Alistair Borthwick:**

586 Conceptualization (equal); Investigation (equal); Writing – review & editing (equal).

587

## 588 DATA AVAILABILITY

589 The data that support the findings of this study are available from the corresponding  
590 author upon reasonable request.

591

## 592 APPENDIX: VALIDATION OF THE CFD MODEL

593 The settling of a solid sphere in quiescent water was experimentally investigated by  
594 Mordant and Pinton<sup>56</sup> who derived the temporal variation in settling velocity from  
595 measurements of the Doppler shift of an ultrasonic wave scattered by a moving particle.  
596 Two cases with  $d_n = 0.5$  mm and 1.5 mm are simulated herein in order to validate the  
597 applied CFD model. The particle density is  $\rho_p = 2560$  kg/m<sup>3</sup>, the water density is  
598  $\rho_f = 1000$  kg/m<sup>3</sup>, and the dynamic viscosity of water  $\mu = 8.9 \times 10^{-4}$  kg/m/s. The  
599 simulation setup is the same as previously described in Sec. II.B except that three mesh  
600 resolutions are tested, i.e.,  $\Delta h = 1/10$ ,  $1/12$ , and  $1/14 d_n$ .

601 Fig. 15 shows that there is good agreement between the simulated and measured  
602 settling velocities, thus validating the model, and demonstrating that a mesh resolution of  
603  $\Delta h = 1/12 d_n$  is sufficiently fine to produce accurate results.

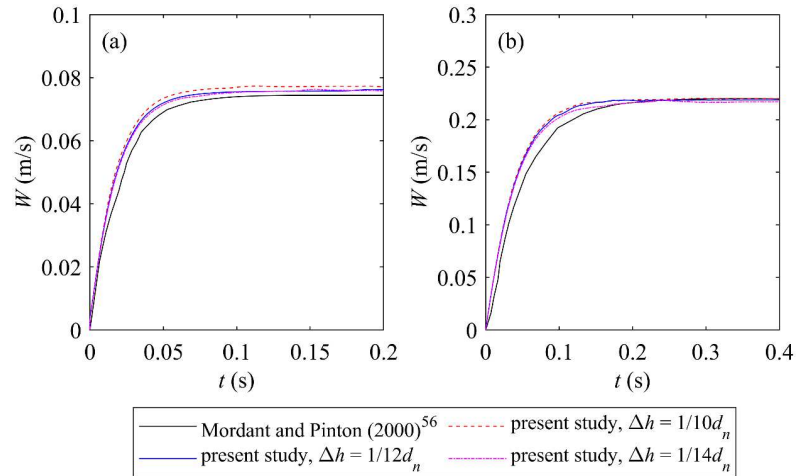
604



This is the author's peer reviewed, accepted manuscript. However, the online version of record will be different from this version once it has been copyedited and typeset.

PLEASE CITE THIS ARTICLE AS DOI: 10.1063/5.0165555

Accepted to Phys. Fluids 10.1063/5.0165555



605

606 **FIG. 15.** Time history of settling velocity  $W$  for spheres of (a)  $d_n = 0.5$  mm and (b)  
 607  $d_n = 1.5$  mm. Black solid line refers to measured data by Mordant and Pinton<sup>56</sup>.

608

609 **REFERENCES**

610 <sup>1</sup>M. Church, “Bed material transport and the morphology of alluvial river channels,”  
 611 *Annu. Rev. Earth Planet. Sci.* **34**(1), 325-354 (2006).

612 <sup>2</sup>S. Dey, A. S. Zeeshan, and E. Padhi, “Terminal fall velocity: the legacy of Stokes from  
 613 the perspective of fluvial hydraulics,” *Proceedings of the Royal Society A* **475**(2228),  
 614 20190277 (2019).

615 <sup>3</sup>I. A. Kane and M. A. Clare, “Dispersion, accumulation, and the ultimate fate of  
 616 microplastics in deep-marine environments: A review and future directions,” *Front. Earth*  
 617 *Sci.* **7**, 00080 (2019).

618 <sup>4</sup>J. Li, E. Shan, J. Zhao, J. Teng, and Q. Wang, “The factors influencing the vertical  
 619 transport of microplastics in marine environment: A review,” *Sci. Total Environ.* **870**,

This is the author's peer reviewed, accepted manuscript. However, the online version of record will be different from this version once it has been copyedited and typeset.

PLEASE CITE THIS ARTICLE AS DOI: 10.1063/5.0165555

Accepted to *Phys. Fluids* 10.1063/5.0165555

- 620 161893 (2023).
- 621 <sup>5</sup>B. R. Barboza, B. Chen, and C. Li, “A review on proppant transport modelling,” *J. Pet.*  
622 *Sci. Eng.* **204**, 108753 (2021).
- 623 <sup>6</sup>S. Yao, C. Chang, K. Hai, H. Huang, and H. Li, “A review of experimental studies on the  
624 proppant settling in hydraulic fractures,” *J. Pet. Sci. Eng.* **208**, 109211 (2022).
- 625 <sup>7</sup>R. P. Chhabra and J. F. Richardson, *Non-Newtonian Flow and Applied Rheology:*  
626 *Engineering Applications* (Butterworth-Heinemann, 2008).
- 627 <sup>8</sup>M. Mandø and L. Rosendahl, “On the motion of non-spherical particles at high Reynolds  
628 number,” *Powder Technol.* **202**, 1-13 (2010).
- 629 <sup>9</sup>H. Ma, L. Zhou, Z. Liu, M. Chen, X. Xia, and Y. Zhao, “A review of recent development  
630 for the CFD-DEM investigations of non-spherical particles,” *Powder Technol.* **412**,  
631 117972 (2022).
- 632 <sup>10</sup>Y. Zhao, P. Zhang, L. Lei, L. Kong, S. A. Galindo-Torres, and S. Z. Li, “Metaball-  
633 Imaging discrete element lattice Boltzmann method for fluid–particle system of complex  
634 morphologies with case studies,” *Phys. Fluids* **35**(2), 023308 (2023).
- 635 <sup>11</sup>R. Clift and W. H. Gauvin, “Motion of entrained particles in gas streams,” *Can. J. Chem.*  
636 *Eng.* **49**(4), 439-448 (1971).
- 637 <sup>12</sup>N. Cheng, “Comparison of formulas for drag coefficient and settling velocity of  
638 spherical particles,” *Powder Technol.* **189**(3), 395-398 (2009).
- 639 <sup>13</sup>A. Terfous, A. Hazzab, and A. Ghenaim, “Predicting the drag coefficient and settling  
640 velocity of spherical particles,” *Powder Technol.* **239**, 12-20 (2013).
- 641 <sup>14</sup>W. E. Dietrich, “Settling velocity of natural particles,” *Water Resour. Res.* **18**(6), 1615-  
642 1626 (1982).
- 643 <sup>15</sup>A. Haider and O. Levenspiel, “Drag coefficient and terminal velocity of spherical and  
644 nonspherical particles,” *Powder Technol.* **58**(1), 63-70 (1989).

This is the author's peer reviewed, accepted manuscript. However, the online version of record will be different from this version once it has been copyedited and typeset.

PLEASE CITE THIS ARTICLE AS DOI: 10.1063/5.0165555

Accepted to *Phys. Fluids* 10.1063/5.0165555

- 645 <sup>16</sup>A. Hölzer and M. Sommerfeld, “New simple correlation formula for the drag coefficient  
646 of non-spherical particles,” *Powder Technol.* **184**(3), 361-365 (2008).
- 647 <sup>17</sup>F. Dioguardi and D. Mele, “A new shape dependent drag correlation formula for non-  
648 spherical rough particles. Experiments and results,” *Powder Technol.* **277**, 222-230  
649 (2015).
- 650 <sup>18</sup>G. Bagheri and C. Bonadonna, “On the drag of freely falling non-spherical particles,”  
651 *Powder Technol.* **301**, 526-544 (2016).
- 652 <sup>19</sup>A. T. Corey, “Influence of shape on the fall velocity of sand grains,” Ph.D. thesis  
653 (Colorado State University, 1949).
- 654 <sup>20</sup>B. J. Connolly, E. Loth, and C. F. Smith, “Shape and drag of irregular angular particles  
655 and test dust,” *Powder Technol.* **363**, 275-285 (2020).
- 656 <sup>21</sup>Y. Li, Q. Yu, S. Gao, and B. W. Flemming, “Settling velocity and drag coefficient of  
657 platy shell fragments,” *Sedimentology* **67**(4), 2095-2110 (2020).
- 658 <sup>22</sup>S. Chien, “Settling velocity of irregularly shaped particles,” *SPE Drill. Complet.* **9**(04),  
659 281-289 (1994).
- 660 <sup>23</sup>X. Song, Z. Xu, G. Li, Z. Pang, and Z. Zhu, “A new model for predicting drag coefficient  
661 and settling velocity of spherical and non-spherical particle in Newtonian fluid,” *Powder  
662 Technol.* **321**, 242-250 (2017).
- 663 <sup>24</sup>R. Büttner, P. Dellino, L. La Volpe, V. Lorenz, and B. Zimanowski, “Thermohydraulic  
664 explosions in phreatomagmatic eruptions as evidenced by the comparison between  
665 pyroclasts and products from Molten Fuel Coolant Interaction experiments,” *Journal of  
666 Geophysical Research: Solid Earth* **107**(B11), ECV 5-1-ECV 5-14 (2002).
- 667 <sup>25</sup>P. Dellino, D. Mele, R. Bonasia, G. Braia, L. La Volpe, and R. Sulpizio, “The analysis  
668 of the influence of pumice shape on its terminal velocity,” *Geophys. Res. Lett.* **32**(21)  
669 (2005).

This is the author's peer reviewed, accepted manuscript. However, the online version of record will be different from this version once it has been copyedited and typeset.

PLEASE CITE THIS ARTICLE AS DOI: 10.1063/5.0165555

Accepted to *Phys. Fluids* 10.1063/5.0165555

- 670 <sup>26</sup>Y. Wang, L. Zhou, Y. Wu, and Q. Yang, “New simple correlation formula for the drag  
671 coefficient of calcareous sand particles of highly irregular shape,” *Powder Technol.* **326**,  
672 379-392 (2018).
- 673 <sup>27</sup>R. Clift, J. R. Grace, and M. E. Weber, *Bubbles, Drops, and Particles* (Academic Press,  
674 New York, 1978).
- 675 <sup>28</sup>E. Loth, “Drag of non-spherical solid particles of regular and irregular shape,” *Powder*  
676 *Technol.* **182**(3), 342-353 (2008).
- 677 <sup>29</sup>M. de Kruijf, A. Sloopman, R. A. de Boer, and J. J. G. Reijmer, “On the settling of marine  
678 carbonate grains: Review and challenges,” *Earth-Sci. Rev.* **217**, 103532 (2021).
- 679 <sup>30</sup>M. Zastawny, G. Mallouppas, F. Zhao, and B. van Wachem, “Derivation of drag and lift  
680 force and torque coefficients for non-spherical particles in flows,” *Int. J. Multiph. Flow*  
681 **39**, 227-239 (2012).
- 682 <sup>31</sup>R. Ouchene, M. Khalij, B. Arcen, and A. Tanière, “A new set of correlations of drag, lift  
683 and torque coefficients for non-spherical particles and large Reynolds numbers,” *Powder*  
684 *Technol.* **303**, 33-43 (2016).
- 685 <sup>32</sup>S. K. P. Sanjeevi, J. A. M. Kuipers, and J. T. Padding, “Drag, lift and torque correlations  
686 for non-spherical particles from Stokes limit to high Reynolds numbers,” *Int. J. Multiph.*  
687 *Flow* **106**, 325-337 (2018).
- 688 <sup>33</sup>R. Ouchene, “Numerical simulation and modeling of the hydrodynamic forces and  
689 torque acting on individual oblate spheroids,” *Phys. Fluids* **32**(7), 073303 (2020).
- 690 <sup>34</sup>F. Carranza and Y. Zhang, “Study of drag and orientation of regular particles using  
691 stereo vision, Schlieren photography and digital image processing,” *Powder Technol.* **311**,  
692 185-199 (2017).
- 693 <sup>35</sup>H. Başağaoğlu, S. Succi, D. Wyrick, and J. Blount, “Particle shape influences settling  
694 and sorting behavior in microfluidic domains,” *Sci. Rep.* **8**(1) (2018).

This is the author's peer reviewed, accepted manuscript. However, the online version of record will be different from this version once it has been copyedited and typeset.

PLEASE CITE THIS ARTICLE AS DOI: 10.1063/5.0165555

Accepted to *Phys. Fluids* 10.1063/5.0165555

- 695 <sup>36</sup>S. Ghosh and P. Yadav, "Study of gravitational settling of single semi-torus shaped  
696 particle using immersed boundary method," *Appl. Math. Comput.* **413**, 126643 (2022).
- 697 <sup>37</sup>D. Hui, Z. Xu, G. Zhang, and M. Liu, "Sedimentation of elliptical particles in Bingham  
698 fluids using graphics processing unit accelerated immersed boundary-lattice Boltzmann  
699 method," *Phys. Fluids* **35**(1), 13330 (2023).
- 700 <sup>38</sup>C. W. Hirt and J. M. Sicilian, "A porosity technique for the definition of obstacles in  
701 rectangular cell meshes," in *International Conference on Numerical Ship Hydrodynamics*,  
702 *4th*, Washington, DC (1985).
- 703 <sup>39</sup>F. Xiao, "A Computational Model for Suspended Large Rigid Bodies in 3D Unsteady  
704 Viscous Flows," *J. Comput. Phys.* **155**(2), 348-379 (1999).
- 705 <sup>40</sup>C. P. Tsai, Y. C. Chen, T. O. Sihombing, and C. Lin, "Simulations of moving effect of  
706 coastal vegetation on tsunami damping," *Nat. Hazards Earth Syst. Sci.* **17**(5), 693-702  
707 (2017).
- 708 <sup>41</sup>A. Kermanpur, S. Mahmoudi, and A. Hajipour, "Numerical simulation of metal flow  
709 and solidification in the multi-cavity casting moulds of automotive components," *J. Mater.*  
710 *Process. Technol.* **206**(1-3), 62-68 (2008).
- 711 <sup>42</sup>X. Zhu, Y. H. Zeng, and W. X. Huai, "Settling velocity of non-spherical hydrochorous  
712 seeds," *Adv. Water Resour.* **103**, 99-107 (2017).
- 713 <sup>43</sup>G. H. Bagheri, C. Bonadonna, I. Manzella, and P. Vonlanthen, "On the characterization  
714 of size and shape of irregular particles," *Powder Technol.* **270**, 141-153 (2015).
- 715 <sup>44</sup>J. Guo, "Motion of spheres falling through fluids," *J. Hydraul. Res.* **49**(1), 32-41 (2011).
- 716 <sup>45</sup>W. W. Rubey, "Settling velocity of gravel, sand, and silt particles," *Am. J. Sci.* **s5-**  
717 **25**(148), 325-338 (1933).
- 718 <sup>46</sup>J. Guo, "Logarithmic matching and its applications in computational hydraulics and  
719 sediment transport," *J. Hydraul. Res.* **40**(5), 555-565 (2002).

This is the author's peer reviewed, accepted manuscript. However, the online version of record will be different from this version once it has been copyedited and typeset.

PLEASE CITE THIS ARTICLE AS DOI: 10.1063/5.0165555

Accepted to *Phys. Fluids* 10.1063/5.0165555

- 720 <sup>47</sup>G. E. Stringham, D. B. Simons, and H. P. Guy, *The Behavior of Large Particles Falling*  
 721 *in Quiescent Liquids* (US Government Printing Office, 1969).
- 722 <sup>48</sup>X. Dong, Y. Gao, and C. Liu, “New normalized Rortex/vortex identification method,”  
 723 *Phys. Fluids* **31**(1), 011701 (2019).
- 724 <sup>49</sup>H. Zhong, S. Chen, and C. Lee, “Experimental study of freely falling thin disks:  
 725 Transition from planar zigzag to spiral,” *Phys. Fluids* **23**(1), 011702 (2011).
- 726 <sup>50</sup>M. N. Ardekani, P. Costa, W. P. Breugem, and L. Brandt, “Numerical study of the  
 727 settling of spheroidal particles,” *Int. J. Multiph. Flow* **87**, 16-34 (2016).
- 728 <sup>51</sup>J. Liu, P. Zhang, Y. Xiao, Z. Wang, S. Yuan, and H. Tang, “Interaction between dual  
 729 spherical particles during settling in fluid,” *Phys. Fluids* **33**(1), 013312 (2021).
- 730 <sup>52</sup>A. A. Zaidi, “Settling characteristics of bidisperse dilute suspension in the vortex  
 731 shedding regime,” *Phys. Fluids* **32**(9), 093310 (2020).
- 732 <sup>53</sup>A. Hamid, A. B. Arshad, S. Mehdi, M. D. Qasim, A. Ullah, J. J. Molina, and R.  
 733 Yamamoto, “A numerical study of sedimentation of rod like particles using smooth profile  
 734 method,” *Int. J. Multiph. Flow* **127**, 103263 (2020).
- 735 <sup>54</sup>A. Esteghamatian, A. Hammouti, M. Lance, and A. Wachs, “Particle resolved  
 736 simulations of liquid/solid and gas/solid fluidized beds,” *Phys. Fluids* **29**(3), 033302  
 737 (2017).
- 738 <sup>55</sup>Y. Yao, C. S. Criddle, and O. B. Fringer, “The effects of particle clustering on hindered  
 739 settling in high-concentration particle suspensions,” *J. Fluid Mech.* **920**, A40 (2021).
- 740 <sup>56</sup>N. Mordant and J. F. Pinton, “Velocity measurement of a settling sphere,” *Eur. Phys. J.*  
 741 *B* **18**(2), 343-352 (2000).
- 742